Hydrodynamics of Countercurrent Two-Phase Flow in a Centrifugal Field

M. A. T. Bisschops, K. Ch. A. M. Luyben, and L. A. M. van der Wielen
Kluyver Laboratory for Biotechnology, Delft University of Technology, 2628 BC Delft, The Netherlands

Centrifugal adsorption technology (CAT) is a new method for continuous adsorption and ion exchange involving countercurrent flow of liquid and micrometer-range adsorbent particles under the influence of a centrifugal force. Due to the fast adsorption kinetics associated with very small particles, CAT leads to extremely compact separation equipment with high capacities and excellent mass-transfer efficiencies. Experimental results on the hydrodynamics of countercurrent flow of solids and liquid in a centrifugal field are discussed in terms of flooding conditions, pressure drops and holdup of the adsorbent particles in the contactor. A model developed based on the relations for homogeneous fluidization under gravity correctly describes countercurrent flow under gravity, but does not correctly describe countercurrent flow in a centrifugal field. In general, observed capacities of this model are higher than estimated. Although the centrifugal force magnifies the apparent density difference between the two phases, the two-phase flow did not seem to exhibit heterogeneous behavior, such as observed in gas-fluidized beds.

Introduction

Centrifugal adsorption technology (CAT) is a new technique for carrying out adsorption and ion-exchange processes (Bisschops et al., 1996a, 1997a). This technique involves countercurrent contact of the process liquid and micrometer-range adsorbent particles in a centrifugal field. The use of very small particles results in a large interfacial area and short distances for diffusion. As a consequence, the mass-transfer kinetics is extremely fast, and CAT equipment can be much more compact than conventional countercurrent processes, which operate either in a fluidized-bed mode under gravity or in a packed-bed mode. A more detailed description of the advantages of CAT over existing techniques can be found elsewhere (Bisschops et al., 1996b, 1997b).

A critical aspect in CAT is the countercurrent movement of very small adsorbent particles and the liquid flow. Since the centrifugal force increases with the radius, the critical condition for countercurrent flow will depend on the centrifugal force at its lowest value, which is at the solids feed position in the contact zone. The relation between the centrifugal force and the flow rates of both the liquid and solid phases has to be known in order to evaluate the hydrodynamic capacity of the rotor. If the liquid flow exceeds a certain maximum, solids will be rejected at the entrance. This phenomenon has been called ''flooding'' (Elgin and Foust, 1950).

As the adsorbent particles move through the countercurrent flow region toward the rim of the rotor, they will experience an increase in the centrifugal force. This may affect the two-phase flow in either of the following two manners:

1. The increase in terminal settling velocity with increasing centrifugal force leads to an increase of the slip velocity between particles and liquid. Since the flow rates of the two phases do not change over the contact zone, this will lead to an increase of the void fraction toward the periphery of the rotor.

2. The increase in the centrifugal force acting upon the particles results in a denser fluidized bed, in which the particles experience more hindrance due to the interparticle interactions. This will lead to a decrease in slip velocity and an increase of particle concentration toward the periphery of the rotor.

The interfacial area in the contactor is directly related to the solids holdup, and thereby strongly influences the mass-

Correspondence concerning this article should be addressed to L. A. M. van der Wielen.

transfer rate. With respect to the overall mass-transfer rate per unit volume of equipment, a high solids holdup is preferred.

On the other hand, the solids holdup also influences the pressure drop over the contactor. The pressure drop has a hydrostatic and a dynamic contribution, which both increase with increased solids holdup. Since the adsorbent consists of extremely small particles, the friction between liquid and solids may be substantial, leading to a relatively high dynamic pressure drop. The hydrostatic pressure drop is a result of the density difference between the suspension in the contact zone and the liquid. Since the centrifugal force is very high, the hydrostatic pressure drop may be high in spite of the short contact zone.

In liquid fluidized systems with large density differences between the particle and liquid phases, heterogeneous behavior can be observed (DiFelice, 1995), as in many gas fluidized systems. It is anticipated that similar heterogeneous fluidization phenomena can occur in centrifugal systems. Here, the action of the centrifugal force is similar to increasing the (apparent) density differences between particles and liquid. As far as is known to the present authors, this has never been reported for centrifugal systems. Since the occurrence of heterogeneous flow may be detrimental to the desired countercurrent flow in CAT, experiments must be carefully checked for a fluidization regime.

This can lead to a heterogeneous two-phase flow, as is often observed in gas fluidized beds. This type of heterogeneous behavior has also been observed for liquid fluidized systems with high-density differences (DiFelice, 1995).

In this article, we investigate the hydrodynamic aspects of the countercurrent two-phase flow in the centrifugal field. This includes the hydrodynamic capacity and the solids holdup, as well as the relation between the pressure drop and void fraction. Moreover, the analysis includes a check whether the two-phase flow in the centrifugal field is homogeneous or heterogeneous.

Theory of Solid–Liquid Two-Phase Flow

Contrary to gas fluidized systems, liquid fluidized beds usually expand homogeneously instead of showing bubbling behavior (Couderc, 1985; DiFelice, 1995). The work on homogeneous liquid fluidized beds is very extensive, and recent reviews are available (DiFelice, 1995).

Yet, since the centrifugal field gives rise to the apparent density difference, a system that exhibits stable homogeneous fluidization under gravity may show heterogeneous behavior in the centrifugal force field. A stability criterion for homogeneous flow was reported by Gibilaro and Hossain (1986). Their approach leads to a fluidization classification chart equivalent to the Geldart-plot for gas fluidized systems. For heterogeneous flow in liquid fluidized systems, no quantitative description has been formulated yet.

Homogeneous fluidization behavior in a centrifugal field

The key parameters in homogeneous fluidized beds are the terminal settling velocity and the influence of hindered settling. It is expected that the influence of the centrifugal force mainly affects the terminal settling velocity, whereas the hindered settling characteristics in a centrifugal field are expected to be similar to those of fluidized beds under gravity.

Terminal Settling Velocity. The terminal settling velocity of a single particle results from the balance between the force acting upon the particle and the friction between the particle and the fluid. The latter depends on the drag coefficient (C_D), which is a function of the particle Reynolds number. Correlations for the drag coefficients are readily available for all flow regimes. Since the force acting upon a particle in a centrifugal field varies with the distance to the axis of rotation, the terminal settling velocity will increase as the particle moves away from the axis of rotation. This is associated with an increase in the Reynolds number of the particle. In this work, we describe the terminal settling velocity of a particle with the relation reported by Dallavalle (1948), which gives an accurate prediction of the drag coefficient over the entire range of Reynolds number. It allows a convenient analytical expression of the Reynolds number at the terminal settling velocity in terms of system properties only, expressed in the Galileo number (Ga)

$$Re_\infty = \frac{\rho_L v_\infty d}{\mu_L} = \left(-3.810 + \sqrt{14.512 + 1.834\sqrt{Ga}} \right)^2, \quad (1)$$

in which μ_L and ρ_L represent the liquid phase viscosity and density, respectively, and d is the particle diameter. The Galileo number is defined as

$$Ga = \frac{d^3 \Delta\rho \rho_L g}{\mu_L^2}. \quad (2)$$

The influence of the centrifugal force is taken into account by replacing the gravitational acceleration (g) with the centrifugal acceleration ($\omega^2 R$). Hence, the Galileo number for a certain two-phase system in a centrifugal force field can be various orders of magnitude larger than under gravity.

It should be noted that some authors refer to the dimensionless group, defined here as the Galileo number, as being the Archimedes number (Riba and Couderc, 1977; Kmiec, 1982). We have adopted the definition of the Archimedes and Galileo number as given by most authors (including Wen and Yu, 1966; Richardson and Jerónimo, 1979; Martin et al., 1981; Khan and Richardson, 1990; DiFelice, 1995).

Hindered Settling. The settling velocity of a particle in a suspension is smaller than the terminal settling velocity of a single particle. This is mainly attributed to interparticle hindrance, leading to an increase in the drag force. A common method for describing the influence of the particle concentration is the correlation that is generally known as the Richardson-Zaki (1954a,b) relation, but which was originally proposed by Lewis and Bowerman (1952)

$$-\frac{u_L}{v_\infty} = \epsilon_L^n, \quad (3)$$

in which u_L represents the superficial velocity of the fluid in the fluidized bed and ϵ_L is the void fraction. The minus sign is included because the terminal settling velocity and liquid flow in a fluidized bed have opposite directions.

Table 1. Richardson-Zaki Power Index (n)

Range	n
$Re_\infty < 0.2$	4.65
$0.2 < Re_\infty < 1$	$4.35\ Re_\infty^{-0.03}$
$1 < Re_\infty < 500$	$4.45\ Re_\infty^{-0.10}$
$Re_\infty > 500$	2.39

The Richardson-Zaki power index n depends on the flow regime, as shown in Table 1. In the original article, the Richardson-Zaki power index was reported to depend strongly on wall effects (Richardson and Zaki, 1954a,b). Such strong wall effects have not been confirmed, however, and it is doubtful whether the ratio between column diameter and particle diameter has any significant influence at all (Di-Felice, 1995). Therefore, Table 1 lists values for the Richardson-Zaki index without wall effects (Foscolo et al., 1983).

In the centrifugal contactor, the void fraction may vary over the contact length. Application of the slip velocity, which is directly related to the void fraction, is therefore more attractive. Since the accuracy of the Richardson-Zaki relation is as good as or better than any of the void fraction functions, this correlation will be used for describing homogeneous countercurrent flow.

Countercurrent Two-Phase Flow. For countercurrent movement between a swarm of particles and a fluid, the particles are moving with a certain velocity relative to the fluid. The analysis presented below is based on the case where the adsorbent has a higher density than the liquid. In this case, the terminal settling velocity follows the direction of the force field (which is downward in the case of gravity force and outwards in case of a centrifugal force). Countercurrent transport thus corresponds to the situation in which $u_L < 0$ and $u_S > 0$.

Mertes and Rhodes (1955a,b) described a comprehensive way of analyzing two-phase flow. The movement of the adsorbent follows from the slip velocity superimposed upon the liquid flow. This can be expressed in terms of a throughput number, which is the following function of the superficial liquid phase velocity and the void fraction

$$\frac{u_S}{v_\infty} = (1-\epsilon_L)\left[\frac{v_{\text{slip}}}{v_\infty} + \frac{1}{\epsilon_L}\frac{u_L}{v_\infty}\right], \tag{4}$$

in which u_S/v_∞ is the solids throughput number, u_L/v_∞ is the liquid-phase throughput number, and v_{slip} is the slip velocity between solids and the liquid phase, which depends on the solids holdup. Application of the Richardson-Zaki relation for the slip velocity in a suspension gives

$$\frac{v_{\text{slip}}}{v_\infty} = \epsilon_L^{n-1}. \tag{5}$$

The theoretical solids throughput number diagram, shown in Figure 1, indicates that countercurrent transport of solids at a certain liquid flow can be obtained at two solids holdups. This is depicted in Figure 2, which shows an enlargement of the countercurrent region. The vertical line, indicating a constant solids throughput number, has two intersections with the constant liquid throughput number line. The top intersection, with relatively high solids holdup, is referred to as the "*N*-phase," and the lower intersection, corresponding to relatively low solids holdup, as the "*P*-phase." This nomenclature is derived from the negative and positive slopes in the throughput diagram (Mertes and Rhodes, 1955a).

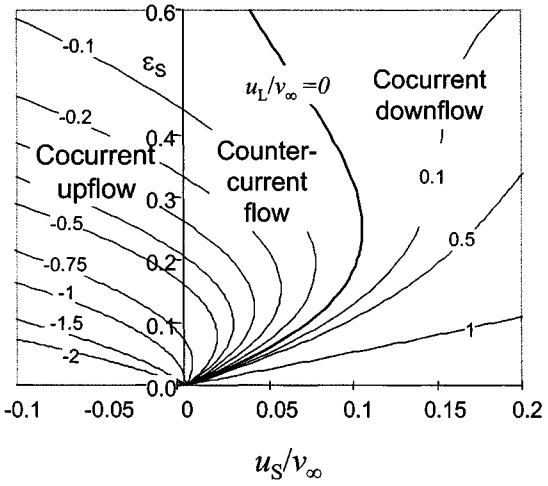

Figure 1. Dimensionless throughput diagram based on Richardson-Zaki relation for hindered settling.

The maximum solids throughput at a given liquid flow rate is calculated using

$$\left[\frac{\partial(u_S/v_\infty)}{\partial\epsilon_L}\right]_{u_L/v_\infty} = 0, \tag{6}$$

from which the flooding relations can be derived. These read (in dimensionless form)

$$\frac{u_S}{v_\infty} = (1-\epsilon_L)^2 n \epsilon_L^{n-1}$$

$$\frac{u_L}{v_\infty} = \left[(1-\epsilon_L)n - 1\right]\epsilon_L^n. \tag{7}$$

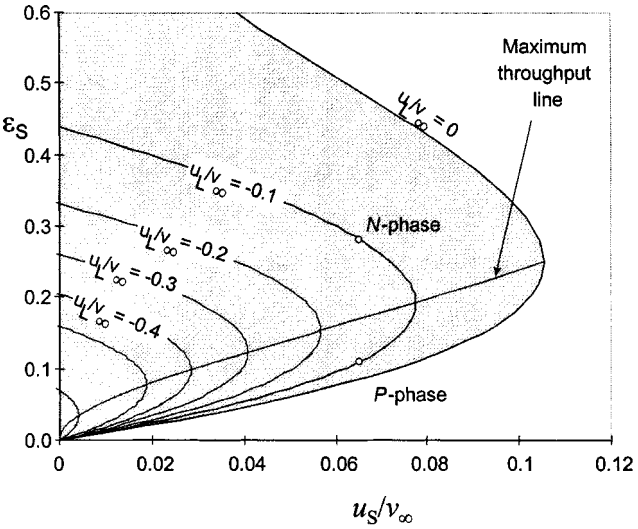

Figure 2. Enlarged countercurrent region of dimensionless throughput diagram.

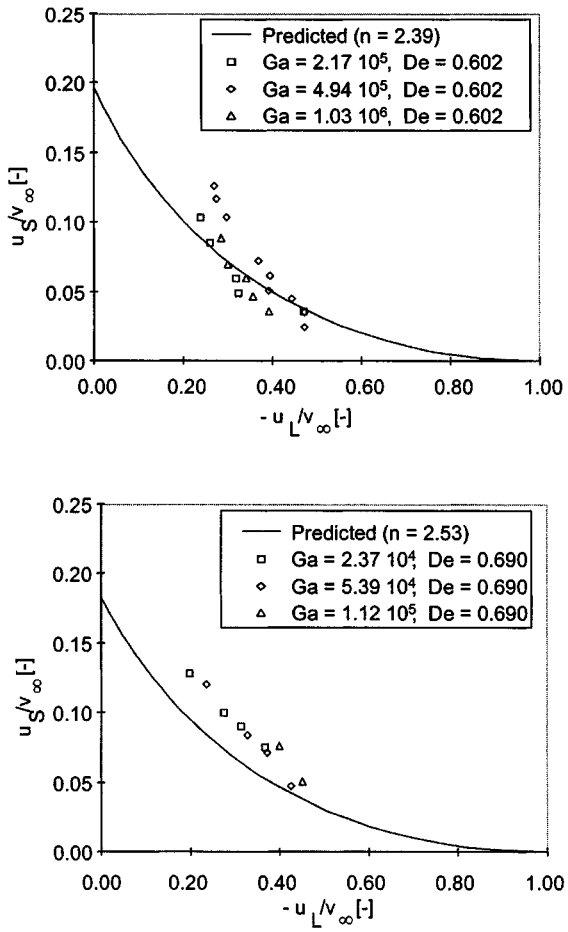

Figure 3. Flooding data for spray tower operations of glass beads ($d = 3.28 - 5.40$ mm; $\rho_S = 1{,}660$ kg/m^3).

Top: In ambient water ($\rho_L = 997$ kg/m^3; $\mu_L = 10^{-3}$ Pa·s); *bottom:* in $MgSO_4$ solution ($\rho_L = 1{,}200$ kg/m^3; $\mu_L = 3 \times 10^{-3}$ Pa·s). Data taken from Elgin and Foust (1950).

Equation 7 relates the maximum throughput of any of the phases in countercurrent flow to the void fraction. The void fraction under countercurrent flooding conditions ranges from $\epsilon_L = (n-1)/n$ at zero liquid flow ($u_L = 0$) to $\epsilon_L = 1$ at maximum liquid flow ($u_L/v_\infty = -1$).

Wallis (1969) agreed with the theoretical flooding relations with experimental flooding data for solid–liquid spray-tower operations, published earlier by Elgin and Foust (1950). These data are shown in Figure 3. The experimental flooding data from Elgin and Foust (1950) are described closely by Eq. 7. More recently, Van der Wielen et al. (1977) reported additional data supporting the flooding criteria.

Rietema (1982) indicated that both the *N*-phase and *P*-phase can be obtained physically. The system will adopt the "free settling state" or "*P*-phase" if the inlet flow rate, rather than the withdrawal rate, of the dispersed phase is limiting, which is the case in spray-tower operations. The "fluidized state" or "*N*-phase" can be obtained if the withdrawal rate, rather than the feed rate, of the dispersed phase is limiting.

In a centrifugal field, the particles experience increasing force as they travel in the direction of the rim. The free settling state, or *P*-phase, corresponds to the situation where an increase in the centrifugal force forces the adsorbent particles to accelerate as they move away from the axis of rotation. This leads to a more open bed. Typically, the predicted solids holdup will range from $\epsilon_S = 5\%$ to 10% at the solids inlet to $\epsilon_S \approx 1\%$ at the rim. In most cases, this is too low to create a reasonable interfacial area, and will thus lead to poor mass-transfer characteristics. In other words, the residence time of the resin particles is too low to allow reasonable mass transfer.

The fluidized state, or *N*-phase, corresponds to the situation in which an increase in the centrifugal force leads to an increase in bed density. The calculated solids holdup ranges from $\epsilon_S = 5\%$ to 10% at the inlet to values up to $\epsilon_S = 40\%$ to 50% at the periphery of the rotor. This yields a large interfacial area, which should result in satisfactory mass-transfer characteristics.

Moreover, the free settling state predicts a two-phase zone, in which the particle concentration and hence the mean density of the suspension decreases toward the periphery of the rotor. This negative density gradient ($\partial\rho/\partial R < 0$) leads to an unstable situation, since it is predicted that the heavier suspension will "float" on top of the lighter suspension. This phenomenon has also been referred to as "Rayleigh instability" (Didwania and Homsy, 1981). The fluidized state, on the other hand, predicts a positive particle density gradient, and hence a positive density gradient ($\partial\rho/\partial R > 0$). The denser region of the two-phase zone is predicted to be located at the rim. As a consequence, this hydrodynamic state is expected to be inherently more stable. It is therefore desired to operate the CAT in the fluidized state rather than in the free settling state. According to Rietema (1982), this can be done by limiting solids flow at the outlet rather than at the inlet.

Pressure drop

The pressure drop in fluidized systems is composed of two contributions that are additive: (1) the dynamic pressure drop due to friction between continuous and dispersed phase, and (2) the hydrostatic pressure. In CAT, the hydrostatic pressure acting upon the rim of the rotor may be high, due to the centrifugal acceleration. Yet, when all flows to and from the rotor are led via the axis of rotation, the hydrostatic pressure difference between liquid in- and outlet is solely determined by the difference in densities between the two-phase region in the contact zone and the liquid in the duct guiding the liquid feed flow toward the rim of the rotor. This hydrostatic pressure difference is written as

$$\Delta P_{\text{stat}} = \Delta\rho\omega^2 \int_{R_i}^{R_o} (1 - \epsilon_L)\, R\, dR, \tag{8}$$

in which the void fraction ϵ_L varies over the column due to the variable centrifugal force, and R_i and R_o represent the solids and liquid feed positions in the contactor, respectively.

For fluidization under gravity, the pressure drop due to friction between particles and liquid is usually omitted. This simplification is valid for relatively large particle diameters,

where the dynamic contribution to the overall pressure drop is small. Yet, as CAT involves movement of very small particles relative to the liquid, the friction between continuous and dispersed phase cannot be neglected. The friction in (liquid and gas) fluidized beds is described using the Ergun relation (1952). This relation includes both the laminar region and turbulent region (Foscolo et al., 1983). For perfectly spherical particles in a contactor with varying void fraction, the Ergun relation is written as

$$\Delta P_{dyn} = \int_{R_i}^{R_o} \left(150 \frac{(1-\epsilon_L)^2}{\epsilon_L^3} \frac{\mu_L u_L}{d^2} + 1.75 \frac{1-\epsilon_L}{\epsilon_L^3} \frac{\rho_L \mu_L^2}{d} \right) dR, \tag{9}$$

in which the first term in the pressure-drop expression is dominant under laminar conditions, while the second term dominates in the turbulent regime. The total pressure drop is the sum of the hydrostatic and dynamic pressure drops

$$\Delta P_{\text{total}} = \Delta P_{\text{stat}} + \Delta P_{\text{dyn}}. \tag{10}$$

Even if the variation of the void fraction over the contactor length is unknown, the pressure drop can be used to estimate the mean void fraction in the contactor.

Experimental Studies

In this work, the following strategy for investigating countercurrent transport between dispersed solids and liquid was adopted:

1. Verification of the homogeneous two-phase flow model under gravity with the following solid phases: relatively large particles (>1 mm) in water with a small density difference; relatively small particles (<100 μm) in water with a large density difference.

2. Verification of the model in the centrifuge, using solid phases in water with different density differences and particle diameters.

Experiments under gravity

Experiments under gravity were performed with two systems: Maxazyme GI Immob. biocatalyst particles in water, and small Ballottini glass beads in tap water at ambient temperature. The relevant properties of the solid phases are given in Table 2. The particle diameters were evaluated using an Image Analysis technique. The averages shown are based on analysis of approximately 100 particles in the case of biocatalyst, and approximately 1000 particles in the case of Ballottini glass beads.

Expansion Behavior. The expansion behavior of the systems was investigated by fluidization experiments in a Perspex column equipped with water manometers at several positions. The inner diameter of the column was 40.5 mm and height was 70 cm. Liquid was fed to the bottom of the column by a peristaltic pump (equipped with Masterflex heads). The liquid flow was monitored by means of a magnetoinductive flowmeter (FlowTec Picomag DMI 6530, range: 0–100 L/h). The glass beads have a density that is large enough to evaluate the void fraction from the pressure drop over the fluidized bed. For the biocatalyst, which has a much lower density, the height of the fluidized bed was used to calculate the void fraction.

Table 2. Physical Properties of the Solid Phase for the Gravity Experiments

System Properties	Maxazyme GI Biocatalyst	Ballottini Glass Beads
Density (ρ_S)	1,100 kg/m^3	2,884 kg/m^3
Particle dia.* (d)	1.30 mm	81.8 μm
Galileo no. (Ga)	2213	10.1
Reynolds no. (Re_∞)	38.8	0.49
Terminal settling vel.** (v_∞)	29.94 mm/s	6.01 mm/s

*Determined by image analysis.
**According to Dallavalle's relation (Eq. 1).

Flooding Experiments. The maximum capacity of countercurrent flow under gravity was investigated in a Perspex column that was equipped with an Elgin-head (Cavers, 1991) at the bottom for solids withdrawal and a fluidized bed directly mounted on top of the bed to ensure maximum throughputs of solids. The layout of the setup is shown in Figure 4, and is very similar to the one described by Mertes and Rhodes (1955a,b) and Elgin and Foust (1950). The liquid is fed to the system by a centrifugal pump (ITT Jabsco 28250-2101, driven by an Electrocraft E26 motor), and the flow is monitored by a magnetoinductive flowmeter (FlowTec Picomag DMI 6530, range 0–100 L/h). In order to ensure proper solids with-

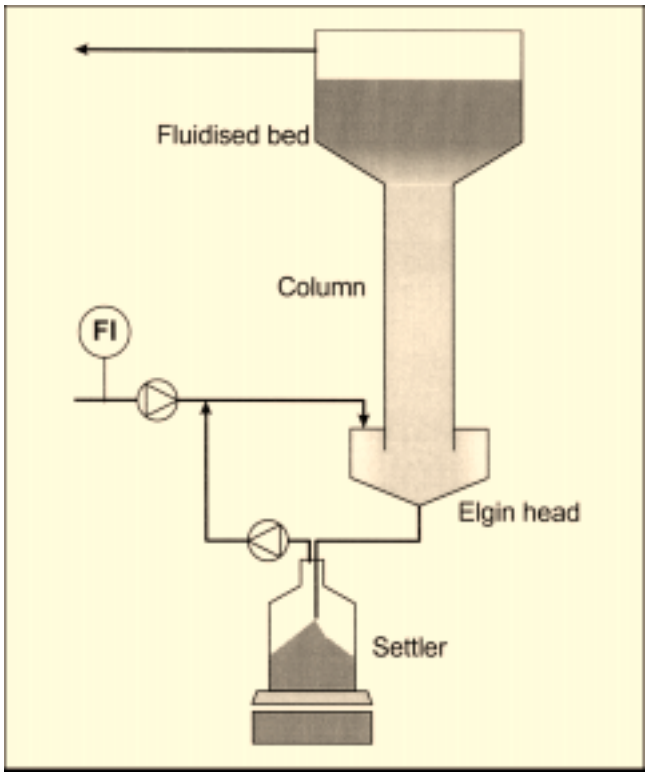

Figure 4. Experimental setup for measuring flooding characteristics under gravity.

drawal at the bottom, a recycle flow was applied over the Elgin-head by means of a peristaltic pump.

The exiting solids were allowed to settle in a flask, which was placed on a balance (Mettler PM 6000), and the volume was kept constant by means of the overflow. The increase in weight of this flask corresponds to the difference between the mass flow of the solids into the flask and the mass flow of liquid out of it. Since these volumetric flows were identical and the densities of both phases were known, the increase in weight allows evaluation of the solids flow rate.

Experiments under centrifugal force

In order to perform experiments under centrifugal force, two experimental set-ups have been constructed at the mechanical workshop of the Kluyver Laboratory for Biotechnology.

Experimental Equipment: The Low-g Rotor. The first rotor consisted of a rotating disc, on which two straight columns were mounted. The rotor was driven by an electromotor and the speed of rotation was measured by a magnetic rotameter and was displayed on the front of the setup. The rotor was contained in a transparent Perspex drum to prevent leakage.

The liquid feed, liquid discharge, and solids feed were directed via the axis of rotation, which was equipped with a rotary seal. The main parts of the setup were constructed from transparent Perspex, to allow visual observations of the two-phase region. A stroboscope was connected to the rotor to ''freeze'' the image of the rotor in one position to facilitate visual observations.

As a consequence of the construction material and the size of the rotor, the speed of rotation was limited to a maximum of $\omega = 250$ rpm (26.2 rad/s). The rotor was therefore referred to as the ''log-g rotor'' (Figure 5). The columns were 30 cm in length and had an inner diameter of $D_c = 25$ mm. The centrifugal acceleration that could be achieved in the column ranged up to 30 g, depending on the solids inlet position. The entire rotor was composed of separate elements, which allows easy exchange modification.

The solids are fed to the rotor as a suspension by a peristaltic pump and enter the column at the inner end via a small pipe. The solids are dragged through the column by the centrifugal force, in the opposite direction to the liquid flow. The liquid feed enters the column at the outer end of the rotor and is pumped toward the axis of rotation by means of a pump. Solids passing the liquid entrance at the outer side of the column are discharged via a nozzle with a little excess of water. In addition to the nozzle discharge, the rotor was also equipped with a tube to guide the slurry effluent backwards to the axis of rotation, from where it is discharged into the drum. The latter will be referred to as ''backflow discharge.'' The system is shown in Figure 6.

In order to maintain the mechanical balance, the rotor is equipped with two columns, which are connected in parallel. During the experiments, it was very difficult to operate the two columns with exactly identical solids discharge rates. As a consequence, the columns operated under different hydrodynamic conditions. Eventually, this may even lead to clogging of one of the two columns. It was therefore decided to disconnect one column and perform the tests with only one column in operation. The second, disconnected column was filled with water in order to maintain the mechanical balance.

The entire setup is shown in Figure 7. The solid phase is fed to the rotor as a slurry from a fluidized bed by means of a calibrated peristaltic pump. Liquid is fed to the rotor by means of a centrifugal pump (ITT Jabsco. 28250-2101; Engine Electrocraft E26). The liquid effluent flows through a 2.5-L settler, in which the solids that have been rejected at the system entrance are collected. This flow is monitored by a magneto-inductive flow indicator (FlowTec Picomag DMI 6530, range: 0–100 L/h). The increase in the mass of the settler is monitored by a balance (Mettler PM 6000), from which the flow rate at flooding can be obtained. The mass increase of the settler is related to the solids flow according to the following relation

$$\frac{dM}{dt} = \phi_S \Delta \rho. \tag{11}$$

The mass balance and flow indicator are connected to a computer for automatic data acquisition. The solids leave the rotor via the solids discharge (either via the nozzle or via the backflow system) in the safety drum, from which they flow to a separate settler.

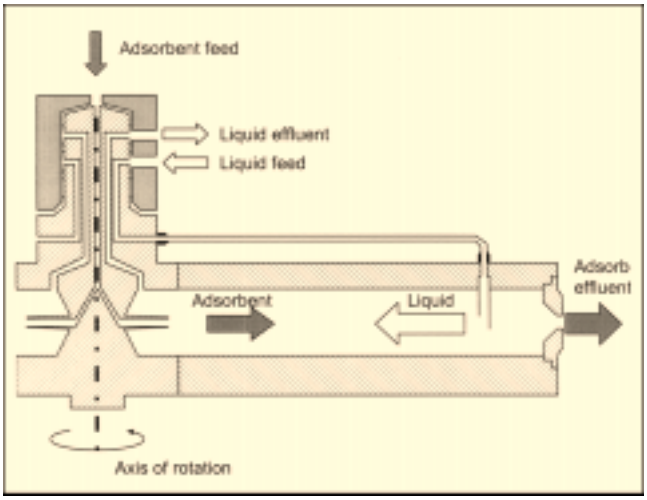

Figure 5. Layout of the low-*g* rotor.

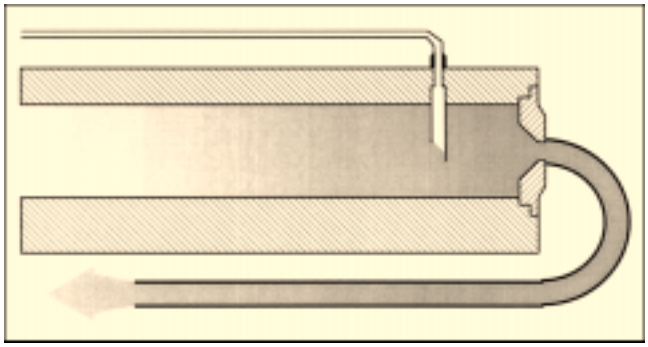

Figure 6. Layout of backflow solids discharge in low-*g* rotor.

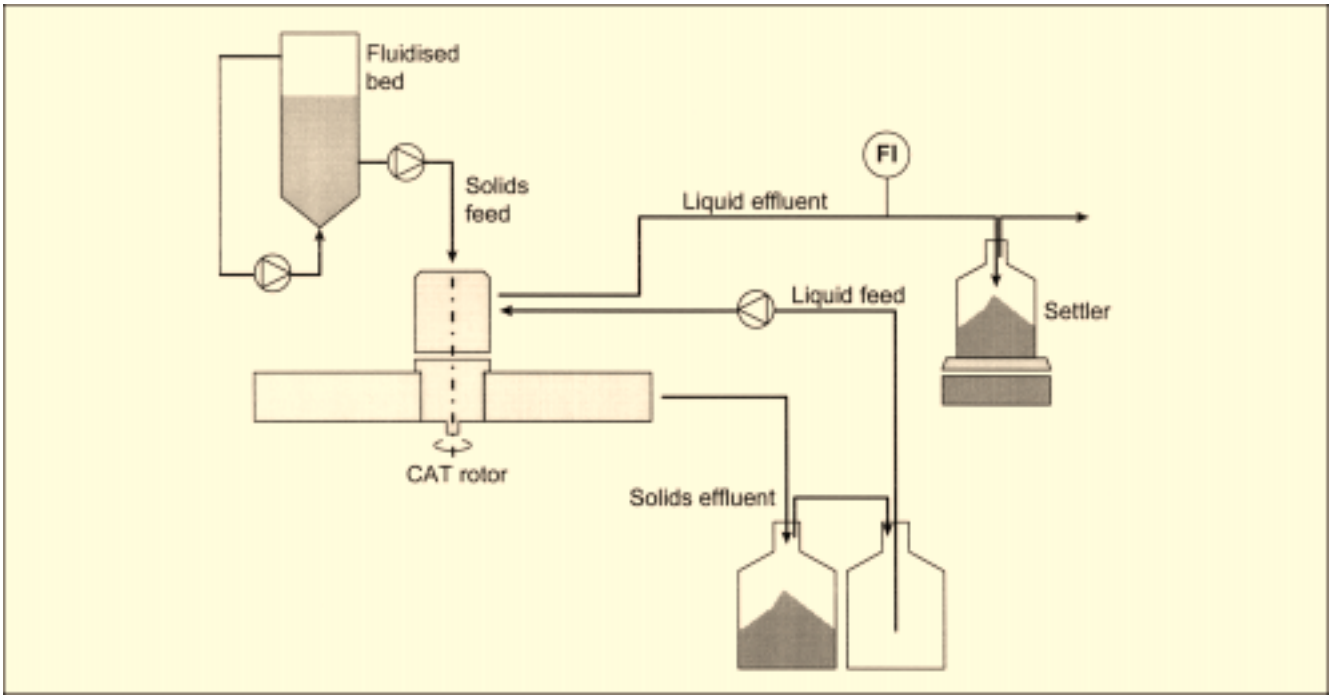

Figure 7. Entire setup for experiments with low-*g* rotor.

Since the liquid flows to and from the rotor also remove the heat produced in the rotary seals, the rotor cannot be operated without water running through the columns. The startup procedure of the setup therefore begins by adjusting the water flow rate through the column by means of the centrifugal pump. Then the speed of rotation is set, and after the rotor has attained the desired speed of rotation, solids are fed to the rotor by switching from liquid to slurry flow. The experimental setup was closed down in reversed order: first the solids flow was switched to water, then the rotor was stopped, and at last the liquid flow is stopped.

Due to the time lag between the discharge from the rotor and from the safety drum, the experimental solids flow through the rotor could not be determined directly. The actual solids flow through the rotor is therefore obtained from the difference between the solids feed flow rate by means of the calibrated pump and the flooding flow rate, obtained from the slope of the mass of the settler.

Experimental Equipment: High-g Rotor. For experiments under higher centrifugal accelerations, a new rotor was constructed. This rotor was constructed of stainless steel, thereby allowing much higher speeds of rotation. This setup, which we will refer to as the ''high-*g* rotor'' (Figure 8), was driven (via a belt) by an electromotor. The motor was electronically controlled and limited to a maximum speed of rotation of $\omega = 2500$ rpm (261.8 rad/s). This setup was also composed of separate elements, each of which could be exchanged or modified easily. Both ends of the axis were equipped with rotary seals. The axis was directed horizontally rather than vertically, and at the rotary seals it was coated with a ceramic top layer in order to avoid excessive abrasion.

Liquid and solids were fed and discharged via rotary seals at the axis of rotation. The rotor is equipped with two straight columns that have an internal diameter of 25 mm and total length of 125 mm. The solids are fed to the rotor in a suspension with approximately 30% solids holdup. The slurry is fed to the column via a little pipe. Liquid is guided toward the outer end of the columns via a little pipe, where it enters the column via the distributor head. Two geometries for the solids discharge and liquid distributor head at the rim of the columns have been tested (Figure 9).

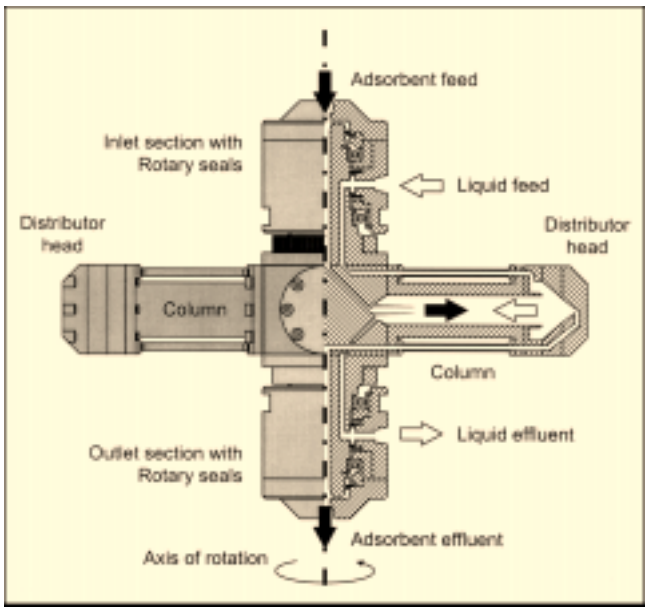

Figure 8. Layout of high-*g* rotor.

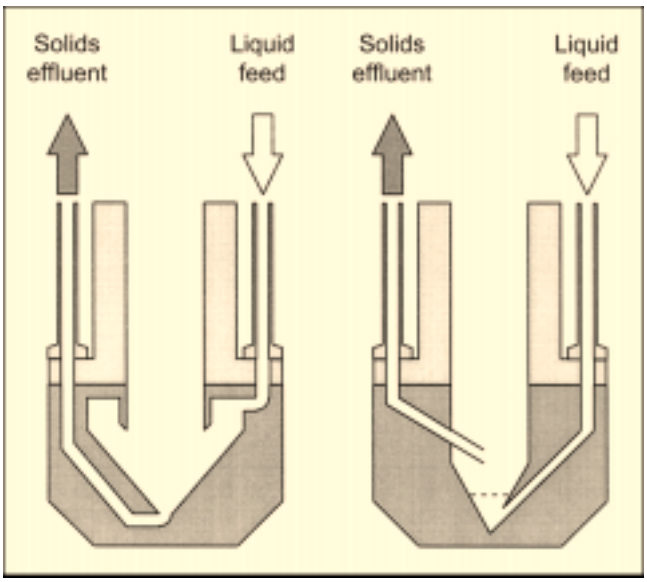

Figure 9. Layout of distributor heads applied in experiments with high-*g* rotor.

Left: The Elgin-head distributor; *right*: the fluidized-bed distributor.

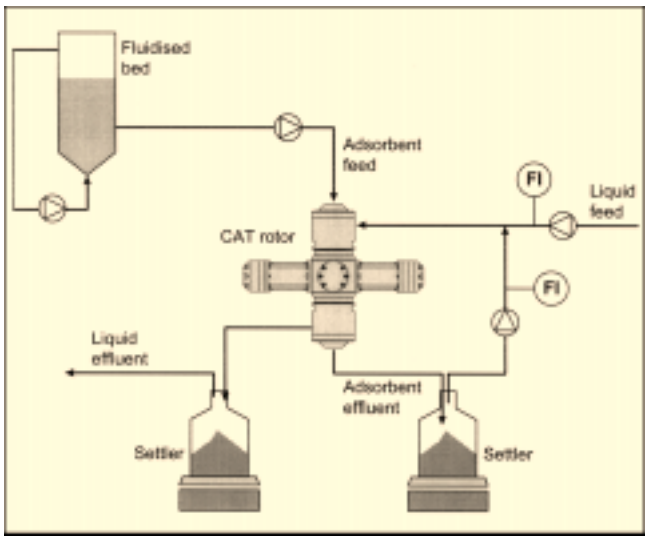

Figure 10. Setup for experiments with high-*g* rotor.

The settler at the liquid effluent has been incorporated in a later stage of the investigations.

• The first distributor was designed such that the solids pass the liquid inlet and are collected and discharged at the periphery of the rotor. In order to obtain stable solids discharge without clogging, the liquid fraction of the solids discharge flow rate should be kept above a certain minimum. Experience showed that the solids holdup in the effluent should not exceed 10 vol. %.

• The second distributor is constructed such that the solids discharge is located closer to the axis of rotation than the liquid feed. As a consequence, this distributor allows the accumulation of a fluidized bed in the contactor, from which a dense slurry can be extracted from the rotor.

The length of the countercurrent contact zone in the two distributors is slightly different. In the case of the first distributor, the entire contact length is measured from adsorbent entrance to liquid entrance: $L_C = 102$ mm. In the case of the second distributor, the contact length is measured from adsorbent entrance to adsorbent withdrawal: $L_C = 110$ mm.

The setup was similar to the one used with the low-*g* rotor (see Figure 10). Since the solids are discharged via the rotary seals at the axis of rotation, the solids flow rate was measured directly. Therefore, the solids were guided through a settler for solid–liquid separation, of which the mass is monitored to determine the solids flow rate. The supernatant is recycled to the rotor via a magneto-inductive flowmeter (FlowTec Picomag DMI 6530, range: 0–50 L/h). The liquid flow rate was monitored by means of a second magneto-inductive flow meter (FlowTec Picomag DMI 6530, range: 0–100 L/h) as well, which was located at the system entrance rather than at the effluent. At a later stage of the experimental work, the setup was also equipped with a pressure-drop meter (range: 0–250 mbar) for monitoring the pressure drop over the liquid in- and outlet. The pressure-drop meter, the flowmeters, and the mass balances are connected to the computer for direct data acquisition.

The startup and close-down procedure was essentially the same as for the low-*g* rotor. When the rotor was equipped with the second distributor, the startup procedure included the formation of the fluidized zone. The accumulation of solids was monitored by means of the pressure-drop meter. If the pressure drop did not indicate a satisfactory accumulation of solids in the rotor. the solids feed rate was somewhat increased.

Initially, the rotor was operated with too high solids feed rates. As a consequence, the rotor would continuously reject solids via the liquid effluent. This method of operation ensures operation in the fluidized state because the solids throughput is limited by the discharge rate rather than by the feed rate. If the solids feed rate was chosen to be lower than the solids discharge rate, the operation may switch toward the fluidized state regime. It should be noted that this point does not necessarily correspond to the maximum throughput at that particular liquid flow rate. The solids discharge rate is controlled by the recycle flow rate rather than by hydrodynamic constraints.

In a later stage of the experimental work, the solids flow rate was controlled on the basis of the pressure drop. As soon as the pressure drop reached its steady-state value during startup, the solids feed rate was controlled such that the pressure drop would remain slightly below that value. As soon as the control algorithm was started, flooding stopped and the liquid effluent was free of solids. A slight increase in the pressure drop set point would then reinitiate flooding.

Model systems

The flooding characteristics of various model systems have been investigated. The relevant physical properties, equipment configuration, and process conditions are listed in Table 3.

Table 3. Conditions for Centrifugal Flooding Experiments

Solid Phase	Setup	Speed of Rotation (rpm)	Ga	Re_∞	v_∞ (mm/s)
Ballottini glass beads	Low-g rotor				
$d = .82$ μm	Nozzle discharge	175 (2.2 g)	22.5	1.01	12.44
$\rho_S = 2{,}885$ kg/m^3	$R_i = 65$ mm				
$De = 0.347$					
Dowex 50 WX8	Low-g rotor	134 (3.01 g)	51.1	2.09	11.03
$d = 190$ μm	Nozzle discharge	150 (3.77 g)	64.0	2.54	13.39
$\rho_S = 1{,}250$ kg/m^3	$R_i = 150$ mm	180 (5.43 g)	92.2	3.45	18.22
$De = 0.80$		200 (6.71 g)	113.8	4.11	21.71
		250 (10.5 g)	177.9	5.92	31.24
	Low-g rotor	150 (4.15 g)	70.4	2.75	14.52
	Backflow	200 (7.38 g)	125.4	4.45	23.48
	$R_i = 165$ mm	250 (11.53 g)	195.7	6.39	33.73
Dowex 50 WX8	High-g rotor				
$d = 90$ μm	$R_i = 72.5$ mm	500 (20.3 g)	43.8	1.83	20.0
$\rho_s = 1{,}250$ kg/m^3		605 (29.7 g)	25.2	1.12	16.09
$De = 0.80$		700 (39.7 g)	85.8	3.25	36.2

Note: The Reynolds number and the terminal settling velocity reported in this table are calculated using Dallavalle's relation (Eq. 1).

Observations and Results

All model systems investigated in this work fall in the completely homogeneous fluidization regime, predicted by Gilibaro and Hossain (1986). As a consequence, the experimental data are compared with the relations, derived for the homogeneous flow description.

Biocatalyst particles in water under gravity

The expansion behavior of the biocatalyst particles in a liquid fluidized bed is shown in Figure 11. It can be described well by the Richardson-Zaki correlation. The terminal settling velocity was extrapolated to $v_\infty = 32.4$ mm/s, and the Richardson-Zaki index was determined to be $n = 2.95$. From the physical properties of the system, the terminal settling velocity was calculated using Eq. 1, resulting in $v_\infty = 29.9$ mm/s (Table 1). Based on the corresponding Reynolds number (Table 1), the Richardson-Zaki index was predicted to be $n = 3.09$. Obviously, the theoretical predictions and experimental results agree very well.

During the flooding experiments, stable countercurrent flow between biocatalyst particles and water was readily obtained. Although a portion of the particles was observed to flow upward close to the wall of the column, the flow of solids was very stable. The maximum throughputs of biocatalyst particles at given water flows are shown in Figure 12. The

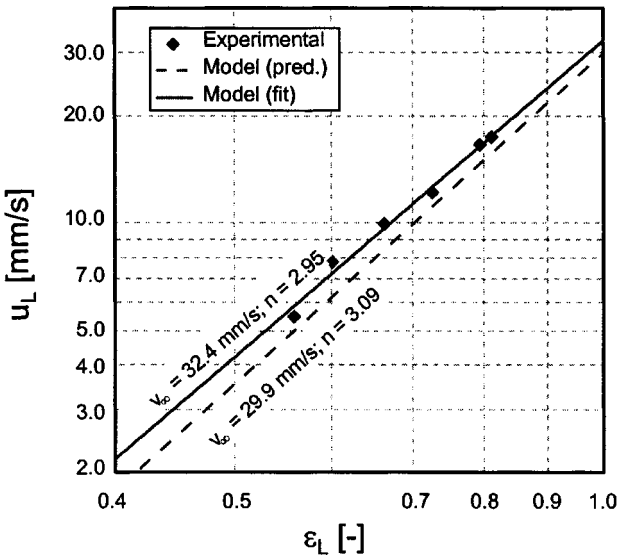

Figure 11. Expansion behavior of biocatalyst particles expressed as fluidization velocity vs. void fraction.

Both curves represent the Richardson-Zaki model (Eq. 3), either with fitted parameters ($v_\infty = 32.4$ mm/s and $n = 2.96$) or with predicted parameters ($v_\infty = 29.9$ mm/s and $n = 3.09$), using Eq. 1 and Table 1.

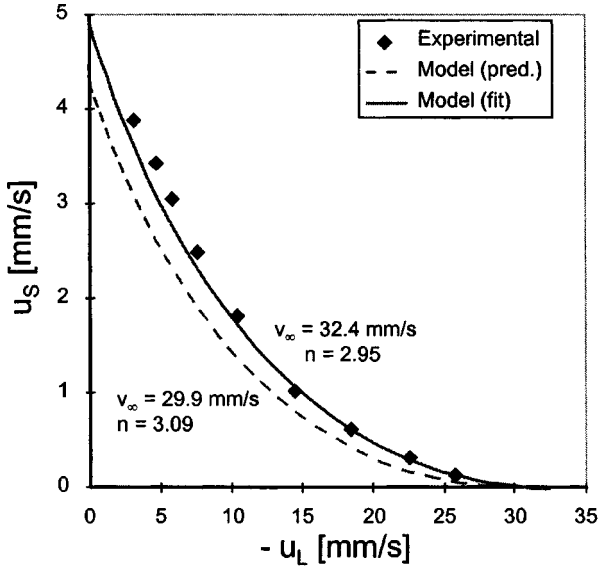

Figure 12. Maximum throughput of biocatalyst particles in a countercurrent fluidized bed as function of the liquid flow rate.

The curves represent the homogeneous flow model (Eq. 7) either with fitted parameters ($v_\infty = 32.4$ mm/s and $n = 2.96$), or with predicted parameters ($v_\infty = 29.9$ mm/s and $n = 3.09$), using Eq. 1 and Table 1.

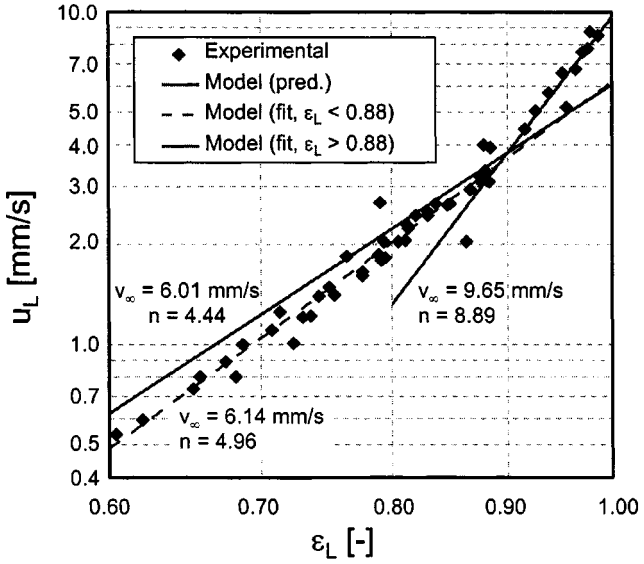

Figure 13. Fluidization of Ballottini glass beads with ambient water: fluidization velocity vs. void fraction.

The curves represent the Richardson-Zaki model (Eq. 3), either with predicted parameters ($v_\infty = 6.01$ mm/s and $n = 4.44$), using Eq. 1 and Table 1, or with fitted parameters ($v_\infty = 6.14$ mm/s and $n = 4.96$ for $\epsilon_L < 0.88$, and $v_\infty = 9.65$ mm/s and $n = 8.89$ for $\epsilon_L > 0.88$).

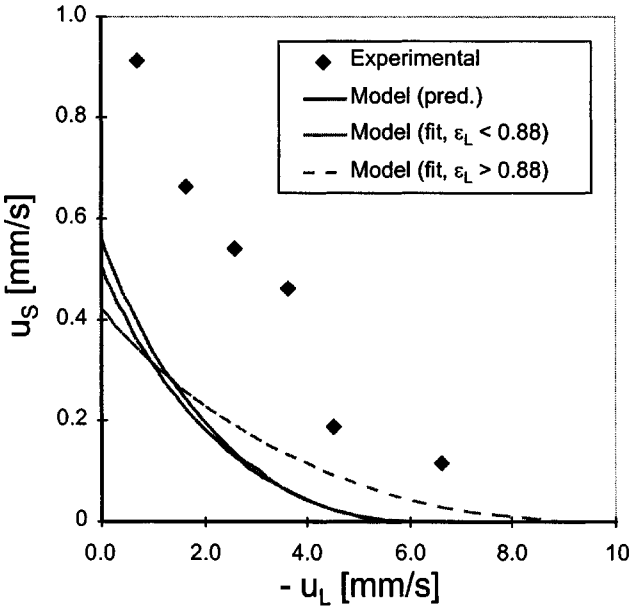

Figure 14. Maximum throughput of Ballottini glass beads in countercurrent contact with ambient water under gravity.

The curves represent the homogeneous flow model (Eq. 7), either with parameters calculated from the physical properties ($v_\infty = 6.01$ mm/s and $n = 4.44$), using Eq. 1 and Table 1, or with parameters fitted to the expansion behavior ($v_\infty = 6.14$ mm/s and $n = 4.96$ for $\epsilon_L < 0.88$, and $v_\infty = 9.65$ mm/s and $n = 8.89$ for $\epsilon_L > 0.88$).

experimental data agree well with the drift-flux model, particularly if the parameters are used that are fitted to the fluidization experiments ($v_\infty = 32.4$ mm/s and $n = 2.95$).

Ballottini glass beads in water under gravity

The expansion behavior of Ballottini glass beads is shown in Figure 13. Two regimes can be distinugished: for more concentrated suspensions ($\epsilon_L < 0.88$), the expansion behavior can be described by the Richardson-Zaki relation, using $v_\infty = 5.95$ mm/s and $n = 4.59$, and for more diluted suspensions ($\epsilon_L > 0.88$), the expansion behavior is described by $v_\infty = 9.65$ mm/s and $n = 8.48$. The predicted terminal settling velocity is $v_\infty = 5.68$ mm/s and the Richardson-Zaki index $n = 4.46$, which corresponds very closely to the fluidization characteristics of the more concentrated suspension. Heterogeneous behavior could not be observed visually, but DiFelice (1995) already argued that visual experiments of glass–water systems can be very deceiving in this respect.

Expansion behavior similar to the curve shown in Figure 13 was found earlier. DiFelice (1995) refers to this type of expansion behavior as *Type II* behavior. The critical value at which the expansion curve switches from the lower linear region toward the higher linear region, corresponds very closely to the values reported in the literature. The transition reported in this work is at $\epsilon_{cr} = 0.88$, whereas Garside and Al-Dibouni (1977) and Riba and Couderc (1977) found $\epsilon_{cr} = 0.85$, while Grbavic et al. (1991) found $\epsilon_{cr} = 0.89$. Rapagna et al. (1989) found that the critical void fraction depended on the particle Reynolds number at its terminal settling velocity, and varied from $\epsilon_{cr} = 0.87$ to $\epsilon_{cr} = 0.97$. In spite of this resemblance, the limiting value for the fluidization velocity at infinite dilution ($\epsilon_L = 1$) does not correspond to the expected terminal settling velocity of a single particle. Due to the very small particle diameter, this parameter is very difficult to access experimentally and it has therefore not been checked. Moreover, the correlation proposed to describe this behavior does not fit the results found in this work.

Similar expansion behavior has been observed for glass beads, with diameters in the range $d = 0.50$–5.0 mm, in water (Wilhelm and Kwauk, 1948). Closer observation of their results indicates that their experimental data could not be described correctly by the relations mentioned earlier either. The particle diameters employed in their experiments, however, led to relatively high Galileo numbers, which are close to the first instability criterion predicted by Gibilaro and Hossain (1986).

During the flooding experiments of Ballottini glass beads and water, the countercurrent flow exhibited large inhomogenities. It was clearly visible that the solid particles did not move individually through the liquid, but flowed through the column in volume elements of dense slurry. These volumes displaced volumes of the less concentrated suspension, which caused the formation of vortices with the size of the column width. These eddies vanished and were formed at time intervals of a few seconds. A smooth homogeneous countercurrent flow of glass beads could not be obtained, irrespective of the startup procedure. The flooding characteristics are shown in *Fout! Verwijzingsbron niet gevonden.*, including predictions based on the fluidization experiments. Neither of the curves corresponding to any of the regimes mentioned earlier correctly predicts the maximum throughput of glass beads. In

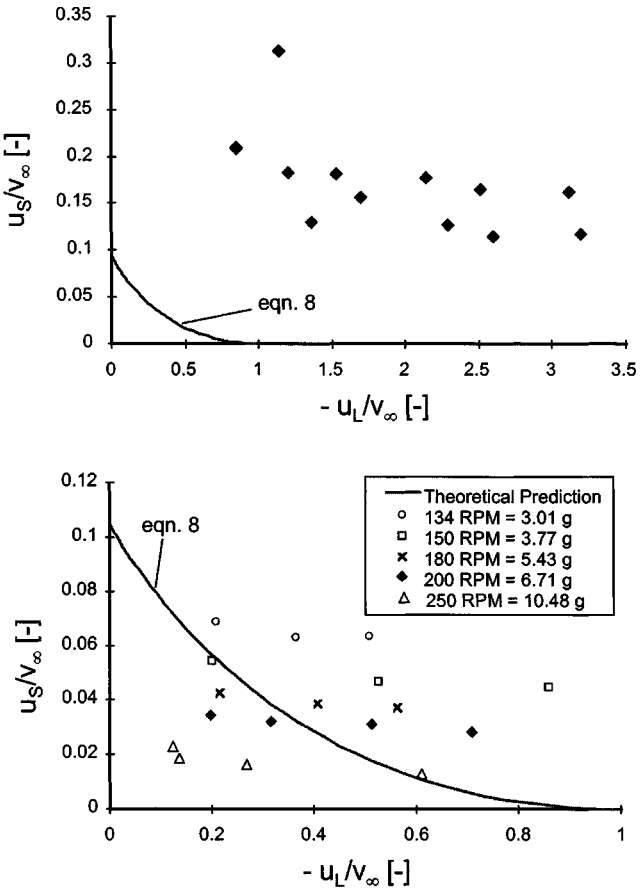

Figure 15. Experimental flooding data obtained in the low-*g* rotor with nozzle discharge.

Top: Glass beads in water at 175 rpm ($d = 82$ μm, $\rho_S = 2{,}885$ kg/m^3, $\omega^2 R_i = 2.2$ g); *bottom:* resin particles in water at various speeds of rotation ($d = 190$ μm, $\rho_S = 1{,}250$ kg/m^3). The model curves are based on Eq. 7, with parameters calculated using Eq. 1 and Table 1 (in the top graph: $n = 4.4$ and in the bottom graph: $n = 4.0$, which is an average value because the actual Richardson-Zaki exponent ranges from $n = 3.7$ to 4.4 for the experiments reported in this graph).

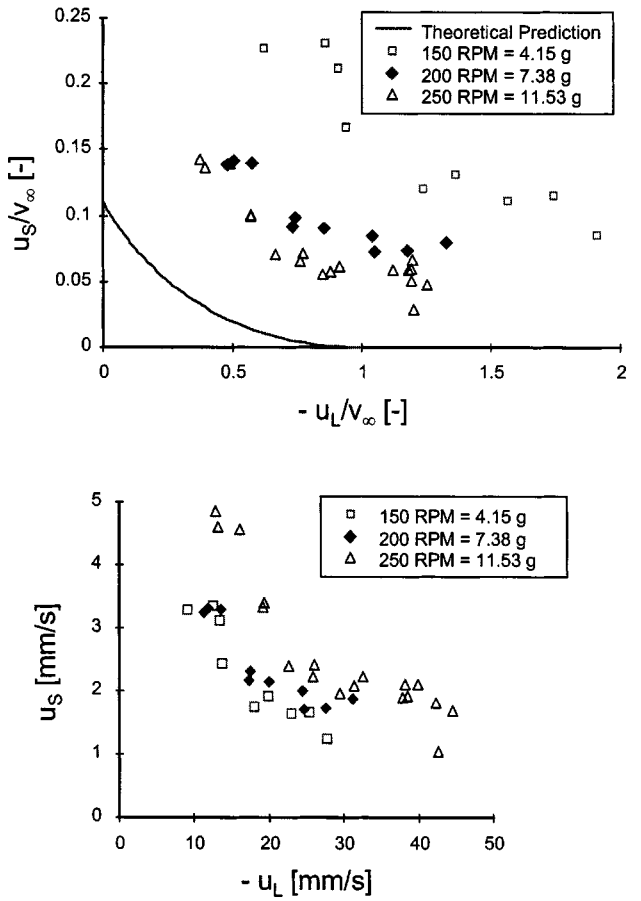

Figure 16. Experimental flooding data for ion-exchange resin ($d = 190$ μm, $\rho_S = 1{,}250$ kg/m^3) in the low-*g* rotor with backflow of the solids discharge.

Top: Expressed in dimensionless throughput numbers; *bottom:* in dimensional form. The curve in the top graph represents the homogeneous flow model (Eq. 7), with the parameters as calculated on base of the physical properties, using Eq. 1 and Table 1.

all cases, the capacity of the column was underestimated. Yet, the experimental flooding data seem to follow the same trend as the model predictions.

Observations in the low-g rotor

The maximum throughputs in the low-*g* rotor have been measured using the systems listed in Table 3 and the configurations discussed before. In all situations, the solids concentration at the discharge was very low (estimated to be less than 5 vol. %).

The results of the experiments with nozzle discharge are shown in Figure 15. The maximum throughput diagram for Ballottini glass beads shows much higher capacities than expected on the basis of the terminal settling velocity of a single particle at the solids inlet position. The capacity of the low-*g* rotor with nozzle discharge for resin particles is on the same order of magnitude as predicted. Yet, the dependence on the liquid flow rate is less than predicted by the homogeneous flow description. Obviously, the capacity on which the homogeneous flow model is based is determined by other phenomena than force balance.

The capacity of the low-*g* rotor has also been tested with backflow of the solids discharge. The density of the slurry was regulated by the back pressure by adjusting the effluent position of the backflow system. Controllable steady-state countercurrent flow operation was thus obtained.

The experimental results and the prediction on the basis of the homogeneous flow description is shown in Figure 16. The capacity of the rotor is clearly higher than might be expected on the basis of the homogeneous flow description. Qualitatively, the experimental data show the same trend as the model predictions.

Visually, no maldistribution or inhomogeneities were observed in the two-phase flow region. Yet, since the visual investigations were very cumbersome due to the high frequency of the stroboscope (2–4 Hz), no definite conclusions can be drawn from these observations.

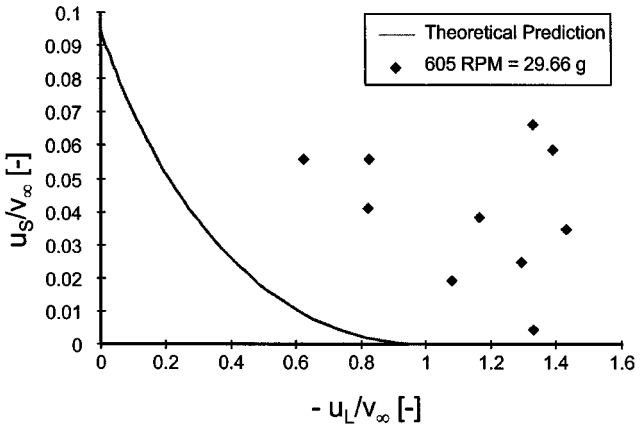

Figure 17. Maximum throughput of resin particles vs. water flow in the high-*g* rotor in the free settling state.

The prediction is based on Eq. 7 with parameters calculated using Eq. 1 and Table 1 ($v_\infty = 16.09$ mm/s and $n = 4.65$).

Observations in the high-g rotor

Flooding experiments in the high-*g* rotor have been done with the first (Elgin-head) distributor only. These are shown in Figure 17. When the rotor was equipped with the fluidized-bed distributor, solids were allowed to accumulate in the rotor leading to the formation of a fluidized bed. After a certain period the fluidized zone apparently reached the solids inlet position and eventually the liquid outlet position. At that moment, solids started to leave the rotor via the liquid effluent. It was impossible to distinguish whether the (controlled) solids discharge rate or the hydrodynamic capacity of the rotor was limiting. As a consequence, the maximum throughput of the high-*g* rotor equipped with the second distributor could not be investigated.

The capacity data for this configuration also have been plotted in Figure 18 and Figure 19, and they show that operation beyond the predicted maximum flow was obtained. The difference in pressure drop between an empty column (evaluated after the close-down procedure in order to eliminate the influence of the small particles in the outermost cone of the contactor) and a column with fluidized bed was used to estimate the mean void fraction in the column by solving the pressure-drop relation (Eq. 12). The results are shown in Figures 18 and 19. The void fractions in the column vary in a narrow range: $\epsilon_L = 0.70-0.80$, irrespective of whether the operation is below or beyond the predicted maximum for homogeneous two-phase flow.

Figure 18 shows that if the rotor is operated above the predicted maximum throughput curve, the void fraction tends to increase slightly as the flow rate of the solid phase increases. Figure 19 shows the opposite trend for operation below the predicted maximum throughput.

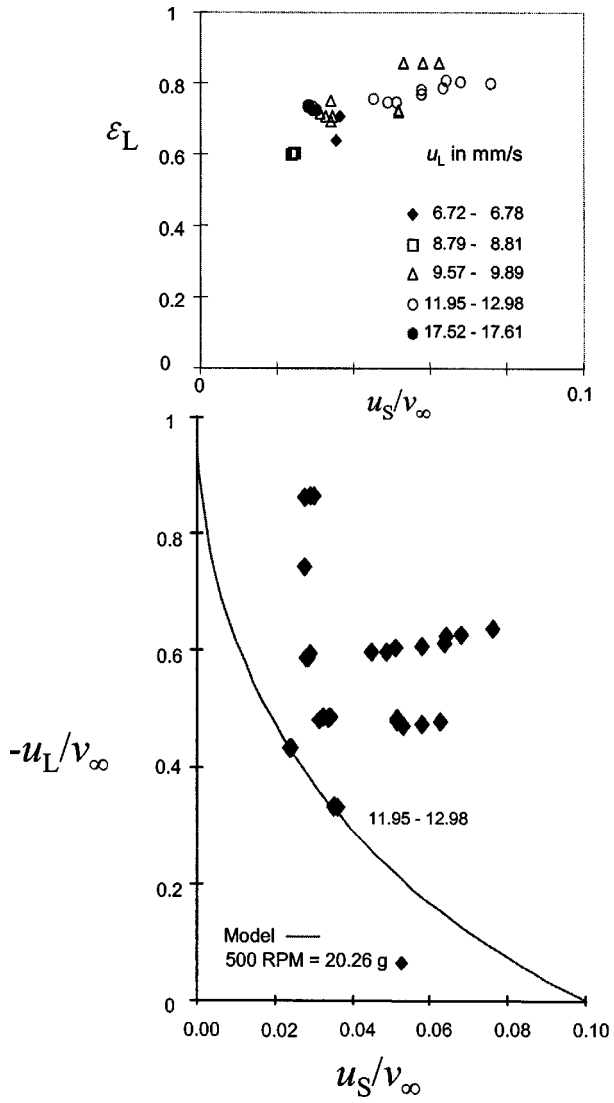

Figure 18. Experimental results obtained in the high-*g* rotor in fluidized state under overload conditions at 500 rpm (20.26 g).

Left: Maximum throughput of the adsorbent vs. the liquid flow. The prediction is based on Eq. 7, with parameters calculated using Eq. 1 and Table 1 ($v_\infty = 20.0$ mm/s and $n = 4.65$). *Right:* Void fraction estimated from the pressure drop (Eq. 10).

Discussion and Conclusions

A model is presented for describing countercurrent two-phase flow under centrifugal conditions. This model is based on homogeneous two-phase flow conditions. The model has been validated under gravity conditions, and it was found that for systems with relatively low-density differences between dispersed and continuous phase, the model can describe the observations very accurately. For small Ballottini glass beads that have a larger density difference with water, the model fails to describe the countercurrent flow accurately. Large inhomogeneities were observed in this system, although it does meet the stability criterion given by Gibilaro and Hossain (1986). These instabilities were not observed during the fluidization experiments of the Ballottini glass beads, although at a higher bed expansion, the expansion characteristics show significant deviations from regular Richardson-Zaki fluidization behavior.

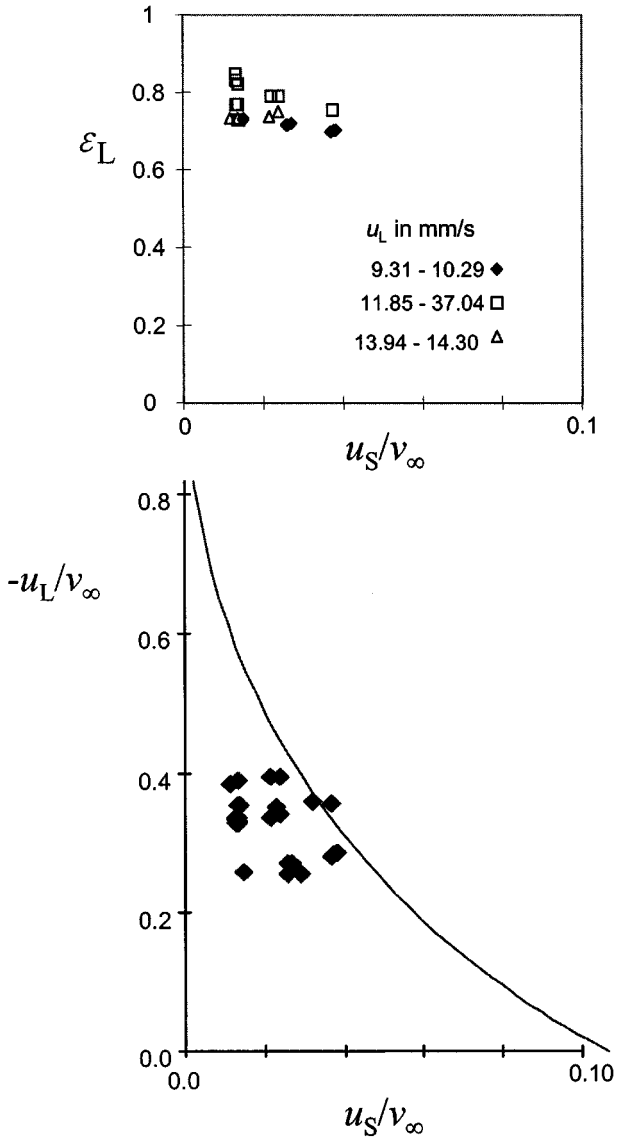

Figure 19. Experimental results from high-*g* rotor in fluidized state with pressure-controlled solids feed at 700 rpm (39.71 g).

Left: Maximum throughput of the adsorbent vs. the liquid flow. The model prediction is based on Eq. 7, with parameters calculated using Eq. 1 and Table 1 ($v_\infty = 1.27$ mm/s and $n = 4.65$). *Right:* Void fraction estimated from the pressure drop (Eq. 10).

The heterogeneous countercurrent flow of Ballottini glass beads leads to a relatively large volume of elements with higher solids concentration moving downward, thereby displacing the volume elements with a very low solids concentration. This method of transport apparently results in higher throughputs than homogeneous countercurrent flow.

Countercurrent flow in a centrifugal field has been investigated and water found to be feasible. Although the systems investigated in the centrifugal contactors meet the stability criterion for homogeneous fluidization given by Gibilaro and Hossain (1986), the homogeneous flow model that was derived cannot describe the hydrodynamic capacity of the centrifugal rotor. If the rotor is equipped with nozzle discharge, the capacity for the iron-exchange resin, which has a relatively low-density difference with water, has the correct order of magnitude, but does not respond to the predicted influence of the superficial liquid velocity. A possible explanation for the behavior is that the solids throughput depends entirely on the nozzle diameter and the presure drop acting upon the solids discharge. This presumption is supported by the fact that most absolute throughputs of resin particles are in the same range, irrespective of the speed of rotation employed.

The low-*g* rotor equipped with backflow solids discharge also yields much higher capacities than expected. However, the deviations seem to become smaller as the centrigual force increases. A possible explanation for this may be the formation of vortices. Liquid moving inward has a tangential velocity as well as a radial velocity. The tangential velocity should change upon moving inward, because of the column walls. This leads to an acceleration in the direction of the rotation. This effect is referred to as the Coriolis force. The same holds for the solids, although the Coriolis effect is the opposite, leading to an acceleration opposite to the direction of rotation.

These opposite effects, in combination with the straight columns, can cause the formation of vortices. As a consequence, the solids throughput is not governed by the motion of individual particles relative to the liquid, which is the basis for the homogeneous flow description, but by bulk flow of a dense slurry relative to a less concentrated suspension. This effect can be expected to be less sensitive to the speed of rotation than the terminal settling velocity of a single particle. As a consequence, the capacity increases with the centrifugal force, but less so than might be expected on the basis of the terminal settling velocity. This agrees with the results presented in this article.

The low-*g* rotor was operated in the free settling state only. Since the axis was equipped with rotary seals for three flows only, the solids discharge could not be controlled accurately. A consequence of this configuration may have been that the solids holdup over the column length decreases, resulting in an inherent unstable hydrodynamic situation. As a consequence, Rayleigh instabilities may occur, giving rise to heterogeneous flow, and hence leading to higher throughputs than expected for homogeneous countercurrent flow. Yet, visual observation of the two-phase flow regime at frequencies up to 4 Hz did not indicate inhomogeneities.

The capacity of the high-*g* rotor was investigated in the spray-tower regime only. This setup also shows much higher capacities than expected. The alternative configuration was shown to ensure reliable and stable operation in the fluidized regime. It was impossible to investigate the maximum capacity of this configuration. Yet, the high-*g* rotor with the second distributor also has operated beyond the predicted maximum-throughput region.

The stability criterion for fluidized beds as derived by Gibilaro and Hossian (1986) cannot be applied to countercurrent systems. The occurrence of Rayleigh instabilities has been observed for a countercurrently moving system that meets their stability criterion. It is uncertain which mode of transport dominates the countercurrent flow in a centrifugal field. The deviations can be attributed to the instabilities that have been observed under gravity, but might as well be caused by

the vortices, which are a result of the tangential flow of both phases.

These vortices may not appear if the flow is not restricted in tangential direction. For scale-up of the centrifugal adsorption technology (CAT), a contact zone that covers the entire periphery is preferred. If this bowl does not involve radial elements that disturb the tangential flow of liquid and adsorbent, the two-phase flow may become more homogeneous. Although this might lead to a decrease in the capacity of the rotor, it could reduce the degree of backmixing, and thereby improve the overall separation performance of the process.

Acknowledgment

Kluyver Laboratory Workshop is gratefully acknowledged for constructing and maintaining the low-g and high-g rotors. The authors owe thanks to Friso Janmaat, Sadi Gül, and Gido van Riet, who have done part of the experimental work. Stef van Hateren and Joop Houwers also have been very helpful during the experiments. The Dutch Department of Economic Affairs is acknowledged for financially supporting the CAT project in the framework of IOP MT-Prevention.

Notation

d = particle diameter, m
D_c = column diameter, m
g = gravitational acceleration, m/s^2
M = mass, kg
n = Richardson-Zaki index
R = radius in the centrifuge, m
R_i = inner radius in the centrifugal contactor (solids inlet position), m
R_o = outer radius in the centrifugal contactor (solids withdrawal position), m
P = pressure, Pa
t = time, s
u_L = liquid-phase superficial velocity, m/s
u_S = solid-phase superficial velocity, m/s
v_∞ = terminal settling velocity, m/s
v_{slip} = slip velocity, m/s

Dimensionless numbers

Ar = Archimedes number ($d^3\rho_L^2 g/\mu_L^2$ or $d^3\rho_L^2\omega^2 R/\mu_L^2$)
De = density ratio (ρ_L/ρ_S)
Ga = Galileo number ($d^3\rho_L\Delta\rho g/\mu_L^2$ or $d^3\rho_L\Delta\rho\omega^2 R/\mu_L^2$)
Re_∞ = Reynolds number ($\rho_L v_\infty d/\mu_L$)

Greek letters

$\epsilon_L\ \epsilon_S$ = liquid and solids volume fraction
ϵ_{cr} = critical liquid volume fraction in Type II fluidization behavior
$\phi_L\ \phi_S$ = Liquid and solids flow rates, m^3/s
$\rho_L\ \rho_S$ = liquid- and solid-phase density, kg/m^3
μ_L = liquid-phase viscosity, Pa·s
ω = speed of rotation, rad/s

Literature Cited

Bisschops, M. A. T., L. A. M. van der Wielen, and K. Ch. A. M. Luyben, Dutch Patent NL 1 002 569 (1996a).
Bisschops, M. A. T., L. A. M. van der Wielen, and K. Ch. A. M. Luyben, "Operating Conditions of Centrifugal Ion Exchange (CentrIX)," *Ion Exchange, Developments and Applications*, J. A. Greig, ed., IEX'96, SCI, London, p. 297 (1996b).
Bisschops, M. A. T., L. A. M. van der Wielen, and K. Ch. A. M. Luyben, PCT Patent Application, PCT/NL97/00121 (1997a).
Bisschops, M. A. T., L. A. M. van der Wielen, and K. Ch. A. M. Luyben, "Centrifugal Adsorption Technology for the Removal of Volatile Organic Compounds from Water," *Process Intensification in Practice, Applications and Opportunities*, J. Semel, ed., bHr Group, London, p. 229 (1999b).
Cavers, S. D., "Nonmechanically Agitated Contactors," *Handbook of Solvent Extraction*, T. C. Lo, M. H. I. Baird, and C. Hanson, eds., Krieger, New York (1991).
Couderc, J. P., "Incipient Fluidization and Particulate Systems," J. F. Davidson, R. Clift, and D. Harrison, eds., *Fluidization*, 2nd ed., Academic Press, London, p. 1 (1985).
Dallavalle, J. M., *Micromeritics, the Technology of Fine Particles*, 2nd ed., Pitman, London (1948).
Didwania, A. K., and G. M. Homsy, "Rayleigh-Taylor Instabilities in Fluidized Beds," *Ind. Eng. Chem. Fundam.*, **20**, 318 (1981).
DiFelice, R., "Review Article Number 47: Hydrodynamics of Liquid Fluidization," *Chem. Eng. Sci.*, **50**, 1213 (1995).
Elgin, J. C., and H. C. Foust, "Countercurrent Flow of Particles Through Moving Continuous Liquid; Pressure Drop and Flooding in Spray-Type Liquid Towers," *Ind. Eng. Chem.*, **42**, 1127 (1950).
Ergun, S., "Fluid Flow Through Packed Columns," *Chem. Eng. Prog.*, **48**, 89 (1952).
Foscolo, P. U., L. G. Gibilaro, and S. P. Waldram, "A Unified Model for Particulate Expansion of Fluidized Beds and Flow in Fixed Porous Media," *Chem. Eng. Sci.*, **38**, 1251 (1983).
Garside, J., and M. R. Al-Dibouni, "Velocity-Voidage Relationships for Fluidization and Sedimentation in Solid-Liquid Systems," *Ind. Eng. Chem. Process Des. Dev.*, **16**, 206 (1977).
Gibilaro, L. G., and I. Hossian, "Aggregate Behavior of Liquid Fluidized Beds," *Can. J. Chem. Eng.*, **64**, 931 (1986).
Grbavic, Z. B., R. V. Garic, Dz. E. Hadzismajlovic, S. Janovic, D. V. Vukovic, H. Littman, and M. H. Morgan III, "Variational Model for Prediction of the Fluid-Particle Interphase Drag Coefficient and Particulate Expansion of Fluidized and Sedimenting Beds," *Power Technol.*, **68**, 199 (1991).
Khan, A. R., and J. F. Richardson, "Pressure Gradient and Friction Factor for Sedimentation and Fluidization of Uniform Spheres in Liquid," *Chem. Eng. Sci.*, **45**, 255 (1990).
Kmiec, A., "Equilibrium of Forces in a Fluidized Bed—Experimental Verification," *Chem. Eng. J.*, **23**, 133 (1982).
Lapple, C. E., and C. B. Shepherd, "Calculation of Particle Trajectories," *Ind. Eng. Chem.*, **32**, 605 (1940).
Lewis, E. W., and E. W. Bowerman, "Fluidization of Solid Particles in Liquids," *Chem. Eng. Prog.*, **48**, 603 (1952).
Martin, B. L. A., Z. Kolar, and J. A. Wesselingh, "The Falling Velocity of a Sphere in a Swarm of Different Spheres," *Trans. Inst. Chem. Eng.*, **59**, 100 (1981).
Mertes, T. S., and H. B. Rhodes, "Liquid-Particle Behavior: I," *Chem. Eng. Prog.*, **51**, 429 (1995a).
Mertes, T. S., and H. B. Rhodes, "Liquid-Particle Behavior: II," *Chem. Eng. Prog.*, **51**, 517 (1955b).
Rapagnà, S., R. DiFelice, L. G. Gibilaro, and P. U. Foscolo, "Steady-State Expansion Characteristics of Monosized Spheres Fluidized by Liquids," *Chem. Eng. Commun.*, **79**, 131 (1989).
Riba, J. P., and J. P. Couderc, "Expansion de Couches Fluidisées par des Liquides," *Can. J. Chem. Eng.*, **55**, 118 (1977).
Richardson, J. F., and W. N. Zaki, "Sedimentation of a Suspension of Uniform Spheres Under Conditions of Viscous Flow," *Chem. Eng. Sci.*, **3**, 35 (1954a).
Richardson, J. F., and W. N. Zaki, "Sedimentation and Fluidization: I," *Trans. Inst. Chem. Eng.*, **32**, 65 (1954b).
Richardson, J. F., and M. A. da S. Jerónimo, "Velocity-Voidage Relations for Sedimentation and Fluidization," *Chem. Eng. Sci.*, **34**, 1419 (1979).
Rietema, K., "Review Article Number 8: Science and Technology of Dispersed Two-Phase Systems: I and II," *Chem. Eng. Sci.*, **37**(8), 1125 (1982).
Van der Wielen, L. A. M., M. H. H. van Dam and K. Ch. A. M. Luyben, "Trickle Flow of Dense Particles in a Fluidized Bed of Others," *Chem. Eng. Sci.*, **52**, 553 (1997).
Wen, C. Y., and Y. H. Hu, "Mechanics of Fluidization," *Chem. Eng. Prog. Symp. Ser.*, **62**, 100 (1966).
Wallis, G. B., *One Dimensional Two-Phase Flow*, McGraw-Hill, New York (1969).
Wilhelm, R. H., and M. Kwauk, "Fluidization of Solid Particles," *Chem. Eng. Prog.*, **44**, 201 (1948).

Manuscript received Dec. 28, 1999, and revision received Sept. 1, 2000.